

Cislunar SDA with Low-Fidelity Sensors and Observer Uncertainty

Joshua M. Block

Air Force Institute of Technology

David H. Curtis, Robert A. Bettinger, and Adam P. Wilmer

Air Force Institute of Technology

ABSTRACT

With an increased interest in the cislunar domain for both civilian and military applications comes a need for Space Domain Awareness (SDA) of objects in cislunar space. Space-based SDA in cislunar space is challenging in part due to difficulties associated with accurately estimating the position of the observer satellite, which is a requirement for effectively performing the SDA mission. Using multiple observation satellites with lower-fidelity equipment helps alleviate these concerns by aggregating together multiple data sets with higher variance to achieve the same level or better accuracy as compared to fewer higher-quality measurement systems. Earth-Moon periodic orbits are used for the observer constellation with a target spacecraft in a L1 Halo orbit. All orbits are modeled using the circular restricted three body problem (CR3BP). Systems Tool Kit (STK) is used to calculate orbit geometries and angles-only measurements are extracted to simulate observing spacecraft with optical sensors. The measurement data is then processed utilizing an Extended Kalman Filter to estimate the position of the target spacecraft. The analysis focuses on comparing the effectiveness of different numbers of observer spacecraft. The results of this simulation found that the use of a low-fidelity constellation can match the performance achieved by a constellation with higher-fidelity systems.

1. INTRODUCTION

In the over two decades since the turn of the century, space has continued to grow in importance in both civilian and military fields. Today, the public focus on it has risen to a level not seen since the Apollo era of space exploration. With this renewed focus has come a refreshed interest in conducting missions within cislunar space from both governments and private corporations. Look no further than NASA's Artemis program with its first launch of an unmanned space capsule to the Moon, with future plans to send humans back to the lunar surface. The construction of the Lunar Gateway [6] in orbit around the moon to establish a long-term presence demonstrates the importance that the region will play in the years to come. With this increased activity that is set to occur in cislunar space comes a need for tracking all the new objects that will be introduced. An accurate method for conducting both space traffic management and space domain awareness (SDA) will be vital to ensure the longevity of any mission operating in the area.

Conducting effective space traffic management and SDA within cislunar space has been a topic of research receiving increased attention over the past couple of years. Several different methods have been proposed for accomplishing effective SDA within the domain, ranging from a space-based solutions to sensors on the lunar surface, with each having their own advantages and detriments. One promising architecture involves the use of cislunar periodic orbits. This is a large family of orbits that can come in a multitude of different shapes such as those of the Earth-Moon 2:1 resonant orbits [5]. These orbits, along with the transfers needed to enter them [7], have previously been studied for their usefulness within an SDA architecture [5]. Some of the advantages of these orbits include low orbit maintenance requirements and expansive coverage of the cislunar domain.

The periodic orbits used for this study come from previous research conducted into their effectiveness in conducting an SDA mission [11, 12]. Previous work focused on visibility analysis of target spacecraft from the observer constellation, while this work focuses on orbit prediction from two of the periodic orbits analyzed in [12]. The target spacecraft orbit used in this work, also from [11], is a L1 Halo orbit. These orbits were chosen based on the results of [11] detailing the high observability rates of the target from the observer constellation. While periodic orbits were picked for the observer constellation in this study, there are a multitude of different orbits that could and should be investigated. A study done by Folwer [4] looked into observability metrics for SDA of a multitude of different cislunar orbits including

L1 and L2 Lyapunov, L1 and L2 Halo, and L4 planar. Each of these orbit families come with their own advantages and detriments. For example, the Lyapunov family of orbits around L1 and L2 make good potential candidates due to their close proximity to the moon and relative stability, but since they are planar in the synodic reference frame their view of objects on the backside of the moon can be blocked. Another recent study [10] looks into the effectiveness of using an Extended Kalman Filter (EKF) and other Kalman Filters for orbit determination of Near Rectilinear Halo Orbits.

The L1 Halo orbit was selected for the target spacecraft due to its potential use as a staging orbit for lunar missions [9]. The Circular Restricted Three-Body Problem (CR3BP) is utilized as the dynamical model to simulate both the measurement data generated by Systems Tool Kit (STK) and the predicted state of the filter. Measurements are collected as modified right ascension and declination representing optical sensors on each observer spacecraft. Random noise is added to each measurement to represent both observer position uncertainty and sensor quality, with both a high fidelity system and a low fidelity system being represented. Each test case has a varying number of observer spacecraft evenly spaced within its respective constellation. This data will then be input into an EKF to track the position of the target spacecraft over a 15 day period. The results show the position and velocity estimation error across each test case and compare that error between the low and high fidelity sensor cases.

2. METHODOLOGY

2.1 Circular Restricted Three-Body Problem

When modeling orbits in cislunar space, the CR3BP is one of the most common dynamical models. This model treats both the Earth and Moon as point masses with the moon in a circular orbit that rotates around the Earth-Moon barycenter at a constant rate relative to the inertial frame. The spacecraft is assumed to have negligible mass. A synodic reference frame is most commonly used to view the system where the Earth and Moon sit fixed on the x-axis with non-dimensional distances $-\mu$ and $1 - \mu$ respectively from the barycenter of the system. This study uses a non-dimensional mass parameter, μ , found in Table 2 and equations of motion represented in Eq. (1-3):

$$\ddot{x} = x + 2\dot{y} - \frac{(1 - \mu)(x + \mu)}{r_{sat/e}^3} - \frac{\mu(x - 1 + \mu)}{r_{sat/m}^3} \quad (1)$$

$$\ddot{y} = y - 2\dot{x} - \frac{(1 - \mu)y}{r_{sat/e}^3} - \frac{\mu y}{r_{sat/m}^3} \quad (2)$$

$$\ddot{z} = -\frac{(1 - \mu)z}{r_{sat/e}^3} - \frac{\mu z}{r_{sat/m}^3} \quad (3)$$

The distances between the satellite and the Earth and Moon respectively in the synodic reference frame can be represented with Eqs. 4 and 5:

$$r_{sat/e}^2 = (x + \mu)^2 + y^2 + z^2 \quad (4)$$

$$r_{sat/m}^2 = (x - 1 + \mu)^2 + y^2 + z^2 \quad (5)$$

All variables for the equations above are non-dimensionalized with the values found in Table 1. The distance unit (DU) uses the distance between the Earth and Moon while the time unit (TU) is equivalent to the period of the system divided by 2π . The mass unit (MU) is represented by the sum of the Earth and Moon masses. The constants used in conjunction with the CR3BP are found in Table 2 below:

2.2 Measurement Generation

This analysis focused on simulating optical sensors onboard observer satellites. To achieve this, an angles only based measurement system similar to that of an Earth based right ascension and declination was used. The angle measurements were all generated based off a set of unit vectors used to represent the body frame of each observing spacecraft. For the rest of this study, the angles will simply be referred to as right ascension and declination.

Table 1: CR3BP Characteristic Quantities

Parameter	Value
Distance Unit (DU)	390,877.4158212686 km
Time Unit (TU)	4.4527 days
Mass Unit (MU)	6.0459×10^{24} kg

Table 2: CR3BP Constants

Parameter	Value
G	$6.674 \times 10^{-20} \frac{Nkm^3}{kg^2}$
m_e	5.9724×10^{24} kg
m_m	7.346×10^{22} kg
μ	0.012150584673

To create the body frame for each observer a couple of assumptions were made. The z-axis of the body frame was assumed to always be aligned with that of the z-axis of the synodic reference frame. To determine the x-axis of the body frame, it was assumed that the optical sensor is aligned with the x-axis and always pointing towards the L1 Lagrange point. This was chosen as L1 within the CR3BP is an equilibrium point. Since the target spacecraft is in a L1 Halo, it will also stay relatively close to L1 over the 15 day window that the scenario takes place. While this helps to simplify the way measurements are generated, it does create the issue of recording some larger angle measurements that are not possible with the Field of View (FOV) of a real optical sensor. The scope of this research was aimed at a preliminary assessment of orbit prediction from the periodic orbits used and thus the assumption was made that the sensors used have no FOV limitation, and that the vector between the observer and the L1 point represents the camera axis (body frame x-axis) from which the right ascension and declination are measured. Eq. 6 shows the vector that defines the body-frame x-axis in the synodic frame. It is created for each observer with the constant position of L1 subtracted by the position of the observing spacecraft.

$$\rho_{obs/L1} = \begin{bmatrix} 0.8369 \\ 0 \\ 0 \end{bmatrix} - \begin{bmatrix} x_{obs} \\ y_{obs} \\ z_{obs} \end{bmatrix} = \begin{bmatrix} L_x \\ L_y \\ L_z \end{bmatrix} \quad (6)$$

System's Tool Kit (STK) was utilized with a MATLAB interface to generate the position and velocity data of both the observer and target spacecraft. The scenario running in STK generated state data every minute using the CR3BP over a 30 day period. This larger set of data is refined to reflect a time step of 10 minutes between observation over a 15 day simulation window. The purpose of generating the larger data set was to try different combinations of time steps and scenario lengths. The time step of 10 minutes was chosen due to its ability to allow the convergence of the data without prohibitively long computation for the simulation. Using a 15 day simulation window for the scenario allowed for the target spacecraft to complete more than a full period of its orbit and all geometries of the observer constellation to be represented. Fig. 1 shows one of the test cases generated in STK.

Once the state data from STK is imported into MATLAB, the process of generating the angle measurements begins. First, the vector between the observer and target is found with Eq. 7 below:

$$\rho_{obs/targ} = \begin{bmatrix} x_{targ} \\ y_{targ} \\ z_{targ} \end{bmatrix} - \begin{bmatrix} x_{obs} \\ y_{obs} \\ z_{obs} \end{bmatrix} = \begin{bmatrix} \rho_x \\ \rho_y \\ \rho_z \end{bmatrix} \quad (7)$$

Using the vectors found in both Eq. 6 and 7, the angles needed for use as the measurements can be calculated using projections. The angle between the projections of the $\rho_{obs/L1}$ vector and the $\rho_{obs/targ}$ vector onto the x-y plane represents the right ascension angle (α) and can be found from:

$$\alpha = \arccos \frac{L_x \rho_x + L_y \rho_y}{\|\rho_{obs/L1}\| \sqrt{\rho_x^2 + \rho_y^2}} \quad (8)$$

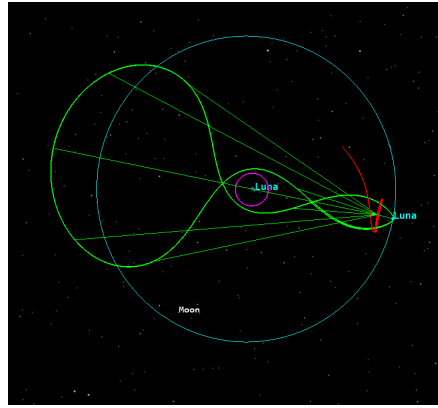


Fig. 1: STK Scenario Example

To get the declination angle (δ), both $\rho_{obs/L1}$ and $\rho_{obs/targ}$ are projected on to the x-z plane. While these angles could also be found solely using $\rho_{obs/targ}$, the projection of both ρ vectors is used so that this measurement system can be more easily modified to accommodate a sensor pointing at any arbitrary point. Eq. 9 shows how the declination angle is calculated:

$$\delta = \arccos \frac{L_x \rho_x + L_z \rho_z}{\sqrt{L_x^2 + L_z^2} \sqrt{\rho_x^2 + \rho_z^2}} \quad (9)$$

The last step for generating the measurements provided to the EKF was to apply random noise. In this study, the measurement noise being applied represents both the uncertainty in sensor measurements and the uncertainty with the position and attitude of the observer. Looking into research with autonav, the ability to self determine trajectory and make maneuvers to hold course, in cislunar space [3] as well as a study looking at expanding spaced-based SDA with expensive and inexpensive sensor systems [8], a metric for determining both the position uncertainty and measurement uncertainty was implemented. Starting with the position uncertainty, based off the uncertainties present when using the autonav method outlined in [3], a position uncertain of 30 km was selected for the expensive, high-fidelity system and 200 km was used for the inexpensive, low fidelity system. These values are the standard deviation, σ_{pos} , for the spacecraft position uncertainty. To convert these into angular uncertainty, the arc length equation (eq. 10) was utilized with 250,000 km as the radius, r , since this is the median range in which measurements will be applied in the filter.

$$\sigma_{pos}^{km} = r \sigma_{pos}^{rad} \quad (10)$$

The angular uncertainty is then converted from radians to arc seconds. In terms of the sensor uncertainty, σ_{sen} , 2 arc seconds was found appropriate for the high fidelity system with 27 arc seconds being used for the low fidelity system. These values were chosen from based off the sensor performance parameters described in [3]. This resulted in total standard deviations that can be found below in Table 3.

Table 3: Measurement Uncertainty in Arc seconds

System	σ_{pos}	σ_{sen}	σ_{total}
High Fidelity	24.7518''	2''	26.7518''
Low Fidelity	165.0118''	27''	192.0118''

2.3 Extended Kalman Filter

With the dynamic model established and the measurements generated, the data can then be passed into the EKF. The EKF is comprised of two parts, the predict stage and the update stage. For the prediction stage, the filter utilizes the CR3BP as the dynamical model and assumes the target spacecraft is not maneuvering. MATLAB's ODE45 is used to propagate the target state vector, \mathbf{X} , with use of the equations of motion as seen in Eq. 1-3 using a time step of 10

minutes. The propagation of the state covariance matrix, \mathbf{P} , is also done using ODE45 and makes use of the Riccati equation found in Eq. 11 below:

$$\dot{\mathbf{P}} = \mathbf{A}\mathbf{P} + \mathbf{P}\mathbf{A}^T + \mathbf{M}\mathbf{Q}\mathbf{M}^T \quad (11)$$

For this equation, \mathbf{Q} represents the dynamic noise present in the system, and \mathbf{M} is simply a sizing matrix for \mathbf{Q} . \mathbf{Q} was adjusted over the course of several test runs to a non-dimensionalized value of 1×10^{-10} which was determined to be an appropriate value for the scope of this test. This number is applied to all states equally and could be further refined to better reflect the inaccuracies associated with the CR3BP but that was not a focus of this research. The matrix \mathbf{A} in Eq. 11 above represents the Jacobian of the dynamics with respect to the state as shown in Eq. 12:

$$\mathbf{A}(t) = \frac{\partial \dot{\mathbf{X}}(t)}{\partial \mathbf{X}(t)} = \begin{bmatrix} a_{11} & a_{12} \\ a_{21} & a_{22} \end{bmatrix} \quad (12)$$

where

$$a_{11} = \begin{bmatrix} \frac{\partial \dot{x}}{\partial x} & \frac{\partial \dot{x}}{\partial y} & \frac{\partial \dot{x}}{\partial z} \\ \frac{\partial \dot{y}}{\partial x} & \frac{\partial \dot{y}}{\partial y} & \frac{\partial \dot{y}}{\partial z} \\ \frac{\partial \dot{z}}{\partial x} & \frac{\partial \dot{z}}{\partial y} & \frac{\partial \dot{z}}{\partial z} \end{bmatrix}$$

$$a_{12} = \begin{bmatrix} \frac{\partial \ddot{x}}{\partial \dot{x}} & \frac{\partial \ddot{x}}{\partial \dot{y}} & \frac{\partial \ddot{x}}{\partial \dot{z}} \\ \frac{\partial \ddot{y}}{\partial \dot{x}} & \frac{\partial \ddot{y}}{\partial \dot{y}} & \frac{\partial \ddot{y}}{\partial \dot{z}} \\ \frac{\partial \ddot{z}}{\partial \dot{x}} & \frac{\partial \ddot{z}}{\partial \dot{y}} & \frac{\partial \ddot{z}}{\partial \dot{z}} \end{bmatrix}$$

$$a_{21} = \begin{bmatrix} \frac{\partial \ddot{x}}{\partial x} & \frac{\partial \ddot{x}}{\partial y} & \frac{\partial \ddot{x}}{\partial z} \\ \frac{\partial \ddot{y}}{\partial x} & \frac{\partial \ddot{y}}{\partial y} & \frac{\partial \ddot{y}}{\partial z} \\ \frac{\partial \ddot{z}}{\partial x} & \frac{\partial \ddot{z}}{\partial y} & \frac{\partial \ddot{z}}{\partial z} \end{bmatrix}$$

$$a_{22} = \begin{bmatrix} \frac{\partial \ddot{x}}{\partial \dot{x}} & \frac{\partial \ddot{x}}{\partial \dot{y}} & \frac{\partial \ddot{x}}{\partial \dot{z}} \\ \frac{\partial \ddot{y}}{\partial \dot{x}} & \frac{\partial \ddot{y}}{\partial \dot{y}} & \frac{\partial \ddot{y}}{\partial \dot{z}} \\ \frac{\partial \ddot{z}}{\partial \dot{x}} & \frac{\partial \ddot{z}}{\partial \dot{y}} & \frac{\partial \ddot{z}}{\partial \dot{z}} \end{bmatrix}$$

The update phase is where the generated measurements are applied to the predicted state. Measurements in this step are only considered if the range from the observer to the target is less than 500,000 km. This metric carries over from the previous work [12] as a value that none of the sensors can see beyond. The first calculation of the update involves solving for the Kalman gain, \mathbf{K} , found with Eq. 13:

$$\mathbf{K} = \mathbf{P}^- \mathbf{H}^T (\mathbf{H}\mathbf{P}^- \mathbf{H}^T + \mathbf{R})^{-1} \quad (13)$$

The superscripts of - and later + are used to denote the state and covariance matrices before and after the update respectively. \mathbf{R} is the measurement noise values found in Table 3. \mathbf{H} is the Jacobian of the measurement model. Since the measurement equations are in terms of the vector between the observer and target, Eq. 14 can be used to construct the \mathbf{H} matrix:

$$\mathbf{H} = \frac{\partial \rho_{obs/targ}}{\partial \mathbf{X}} \frac{\partial \begin{bmatrix} \alpha \\ \delta \end{bmatrix}}{\partial \rho_{obs/targ}} \quad (14)$$

where

$$\frac{\partial \rho_{obs/targ}}{\partial \mathbf{X}} = \begin{bmatrix} 1 & 0 & 0 & 0 & 0 & 0 \\ 0 & 1 & 0 & 0 & 0 & 0 \\ 0 & 0 & 1 & 0 & 0 & 0 \end{bmatrix}$$

$$\frac{\partial \begin{bmatrix} \alpha \\ \delta \end{bmatrix}}{\partial \rho_{obs/targ}} = \begin{bmatrix} \frac{\partial \alpha}{\partial \rho_x} & \frac{\partial \alpha}{\partial \rho_y} & \frac{\partial \alpha}{\partial \rho_z} \\ \frac{\partial \delta}{\partial \rho_x} & \frac{\partial \delta}{\partial \rho_y} & \frac{\partial \delta}{\partial \rho_z} \end{bmatrix}$$

Residuals and measurement Jacobians are used for each observer that can provide a valid measurement. These are used in Eq. 15 and 16 to update the state and covariance:

$$\mathbf{X}^+ = \mathbf{X}^- + K(Meas - z) \quad (15)$$

$$P^+ = P^- - KHP^- \quad (16)$$

This process is repeated across all time steps to have a predicted state and covariance every 10 minutes for the whole 15 day scenario.

3. RESULTS

This work investigated the performance of two different periodic orbits for observers viewing a target in an L1 Halo orbit. The observer periodic orbits come from a previous study [12] examining their feasibility in a SDA architecture based on a target visibility analysis. The target orbit comes from an expanded version of the same study [11]. The initial conditions for these orbits can be found in Table 4:

Table 4: Orbit Non-dimensionalized Initial Conditions in CR3BP

Parameter	Orbit 1	Orbit 2	Target Halo Orbit
x_0	0.993999897750721	0.976500014687630	0.830969944755594
y_0	$-3.7306354 \times 10^{-8}$	0	0
z_0	0	$-1.6769213 \times 10^{-8}$	0.12
\dot{x}_0	0.003741232665221	0.008008641313757	0
\dot{y}_0	-2.122884103965	-1.6768357651	0.234855901450957
\dot{z}_0	0	0	0
T_0	5.4368	12.3287	2.785808231211621

The initial conditions for the orbits used in this study originated from work conducted by Arenstorf [1, 2], but were differentially corrected for a modern mu value [11, 12] as shown in Table 2 such that no propellant would be required to maintain periodicity for 2 full periods in the CR3BP. The L1 Halo orbit starts to develop a divergent trajectory after about a period and a half. However, the divergent behavior does not occur within the 15 day window being simulated in this work. It is assumed that a spacecraft in a L1 Halo orbit would maneuver to remain in the periodic orbit, however this was not simulated in this work. Fig. 2 shows the results of plotting the initial conditions of Orbit 1 and 2 in Table 4 over a full period for each orbit.

Overall, a total of 14 test cases were conducted for the full 15 day scenario. Each test case had 3 main factors that varied between them, observer orbit, number of evenly spaced observers, and system fidelity (sensor/position uncertainty). Test cases are listed in Table 5. The goal of these cases was to determine if a larger constellation of low-fidelity spacecraft could compare to a smaller constellation of high fidelity spacecraft. To this end, the high fidelity test cases include an additional test case for each orbit with a smaller constellation.

One of the assumptions made for this study is that the initial position and covariance are known therefore no initial orbit determination was conducted. The initial state, \mathbf{X}_0 , equalled the initial values for the target provided in Table 4 with no noise added for the first set of test cases. For the initial covariance, P_0 , a starting standard deviation of 10 km

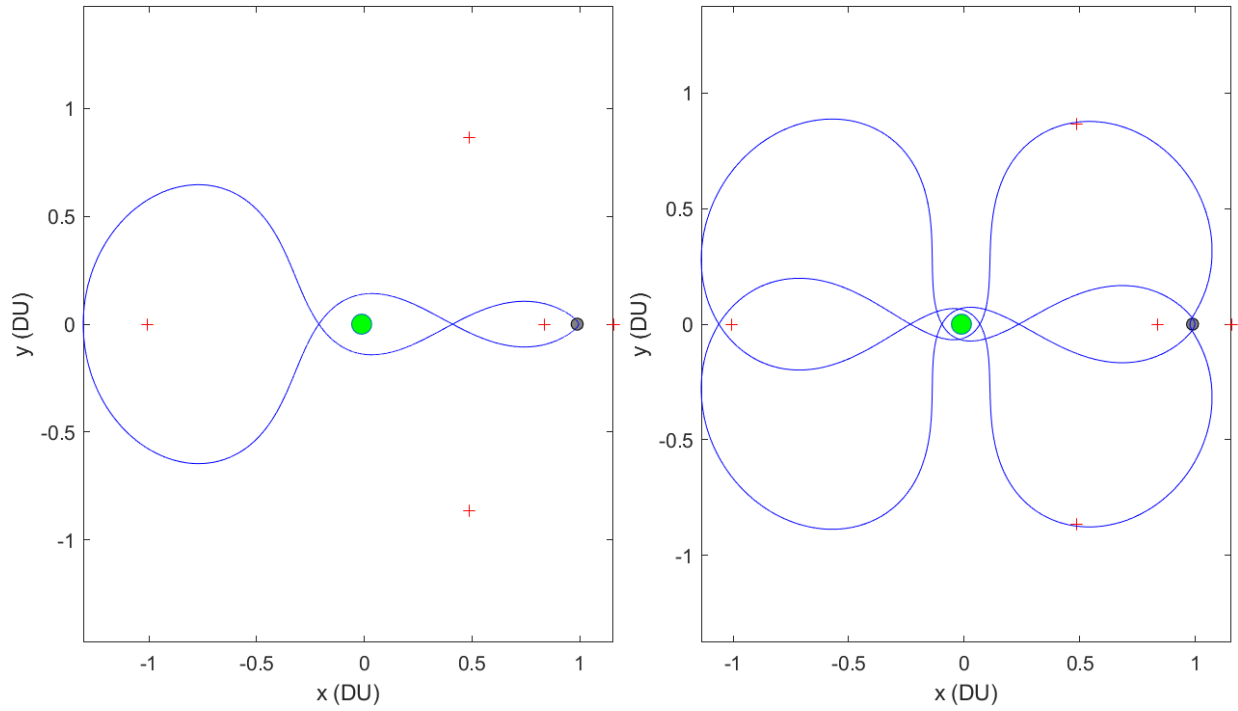


Fig. 2: Observer Orbit 1 and 2 Respectively

Table 5: Test Cases

Case Number	Orbit	Number of Observers	System Fidelity
1	1	4	High
2	1	8	High
3	1	12	High
4	1	16	High
5	2	4	High
6	2	8	High
7	2	12	High
8	2	16	High
9	1	8	Low
10	1	12	Low
11	1	16	Low
12	2	8	Low
13	2	12	Low
14	2	16	Low

was used for the position uncertainty and a 1 m/s standard deviation was used for velocity. These values were chosen using a similar method as used for determining the measurement uncertainties.

3.1 High Fidelity Cases

The high fidelity cases represent the observer spacecraft with high quality equipment for navigation, attitude determination and control, and EO sensing. For Orbit 1, Figures 3-6 show the error between the predicted state and the truth state from the STK data. Figures 7-10 show the error when using Orbit 2:

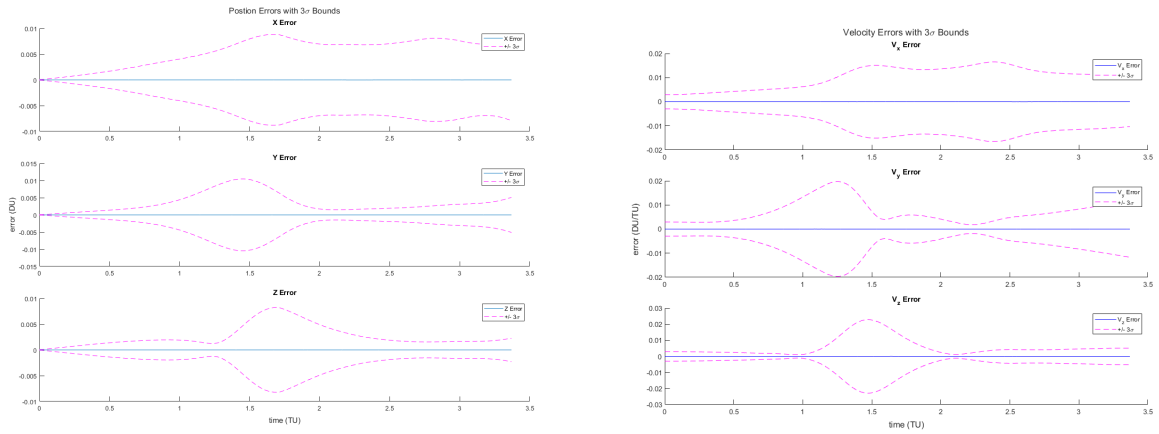


Fig. 3: High Fidelity Error Orbit 1 - 4 Observers

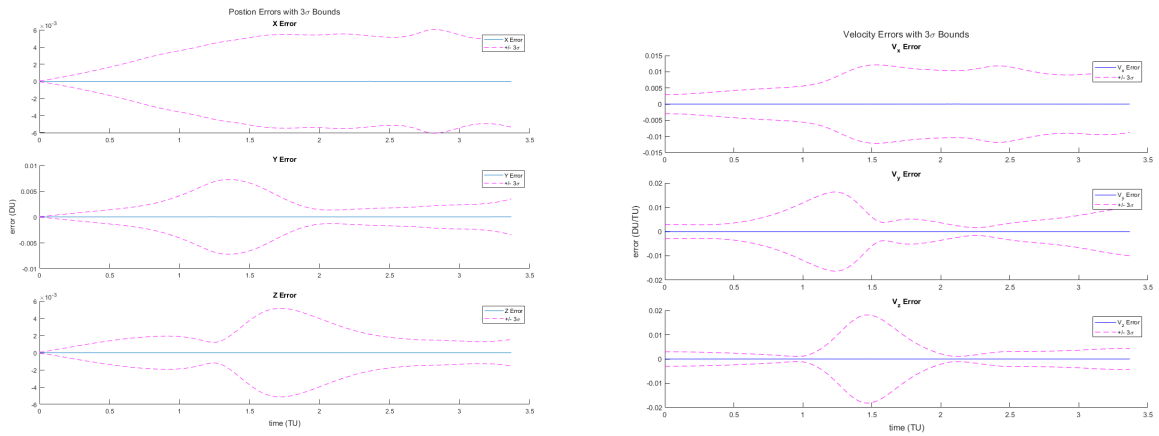


Fig. 4: High Fidelity Error Orbit 1 - 8 Observers

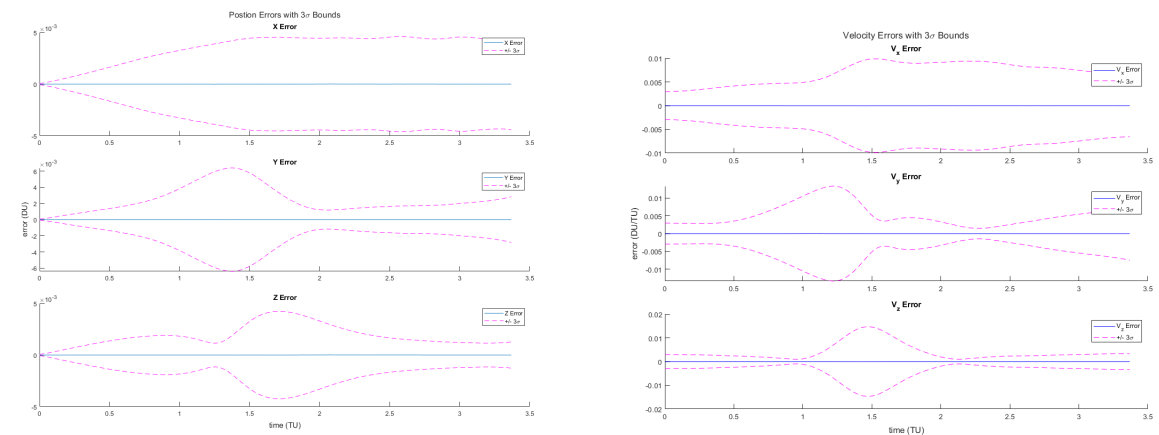


Fig. 5: High Fidelity Error Orbit 1 - 12 Observers

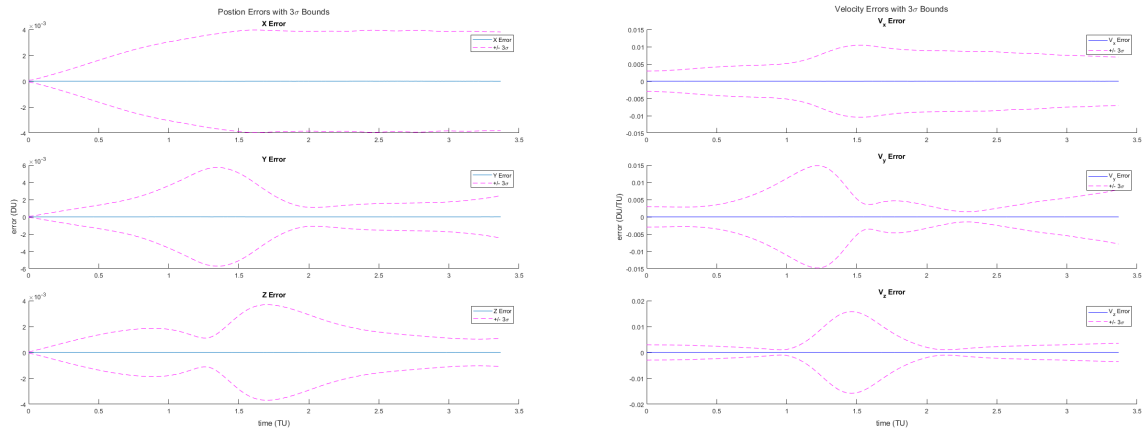


Fig. 6: High Fidelity Error Orbit 1 - 16 Observers

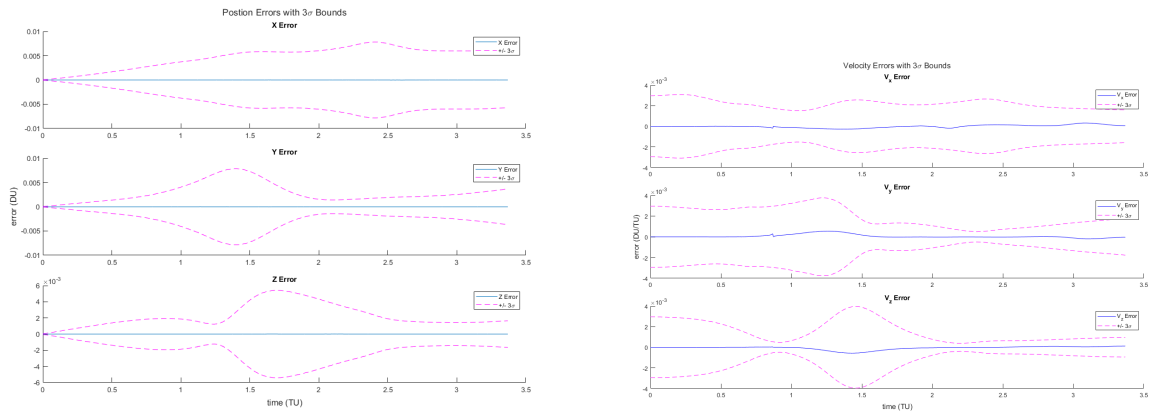


Fig. 7: High Fidelity Error Orbit 2 - 4 Observers

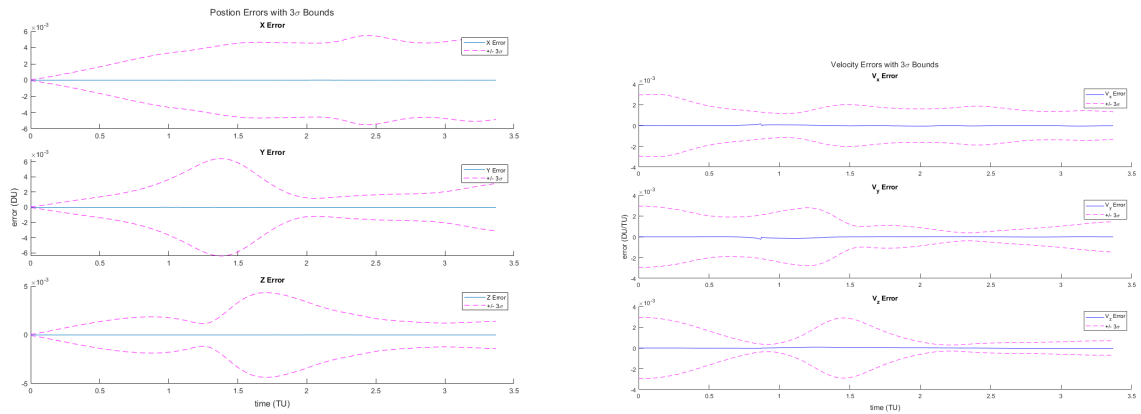


Fig. 8: High Fidelity Error Orbit 2 - 8 Observers

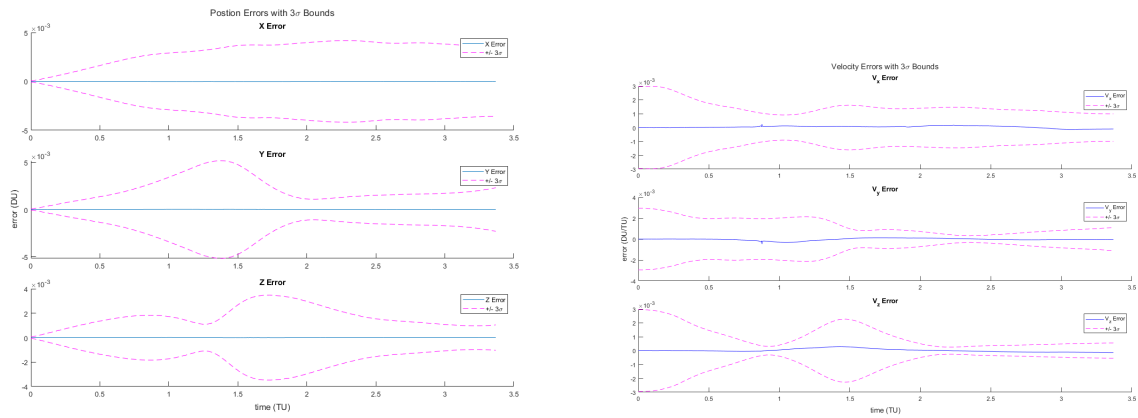


Fig. 9: High Fidelity Error Orbit 2 - 12 Observers

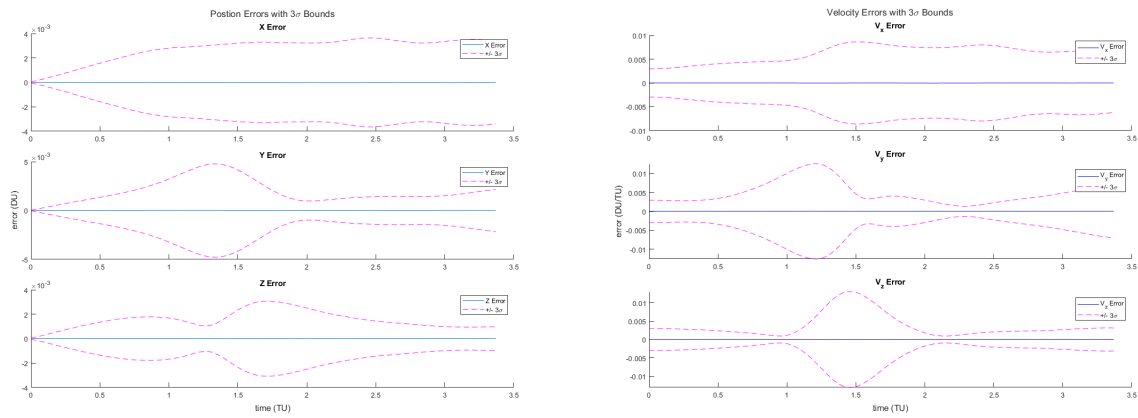


Fig. 10: High Fidelity Error Orbit 2 - 16 Observers

As expected, all 8 test cases representing the high fidelity system are able to accurately predict the satellite over the 15 day window with minimal error. Root mean square error (RMSE) was also found for each case and the results can be found in Table 6:

Table 6: High Fidelity RMSE Values Non-Dimensionalized w/ Conversion

Case	Orbit 1		Orbit 2	
	$RMS_{pos}(km)$	$RMS_{vel}(km/s)$	$RMS_{pos}(km)$	$RMS_{vel}(km/s)$
4 Obs	9.6355e-08 (0.0377)	2.4595e-07 (2.4989e-07)	6.3264e-08 (0.0247)	1.1261e-07 (1.1442e-07)
8 Obs	2.5870e-07 (0.1011)	5.2837e-07 (5.3683e-07)	6.3558e-08 (0.0248)	1.0660e-07 (1.0830e-07)
12 Obs	6.1015e-08 (0.0238)	1.8400e-07 (1.8694e-07)	6.6492e-08 (0.0260)	6.7767e-08 (6.8852e-08)
16 Obs	1.0788e-07 (0.0422)	2.0352e-07 (2.0678e-07)	9.6575e-08 (0.0377)	1.3123e-07 (1.3334e-07)

3.2 Low Fidelity Cases

The low fidelity cases represent the observer spacecraft hosting a lower quality, inexpensive equipment package. For Orbit 1, Figures 11-13 show the error between the predicted state and the truth state from the STK data. Figures 14-16 show the error when using Orbit 2:

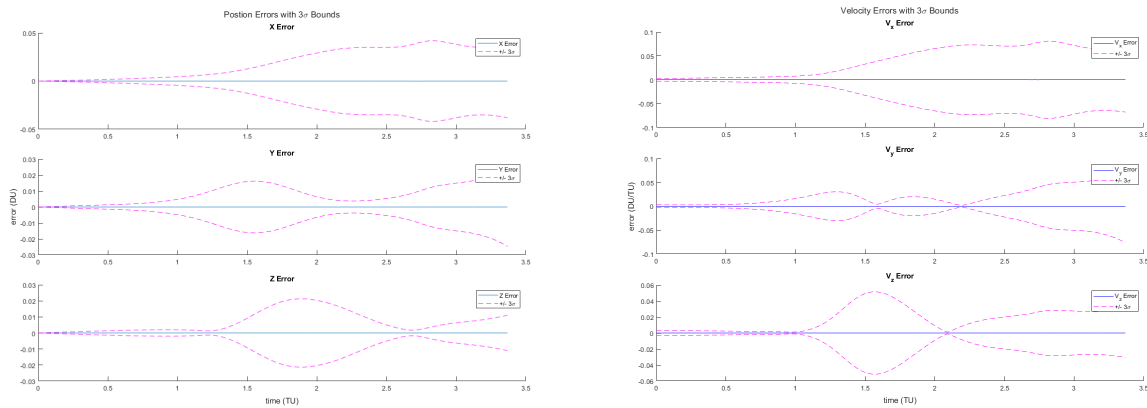


Fig. 11: Low Fidelity Error Orbit 1 - 8 Observers

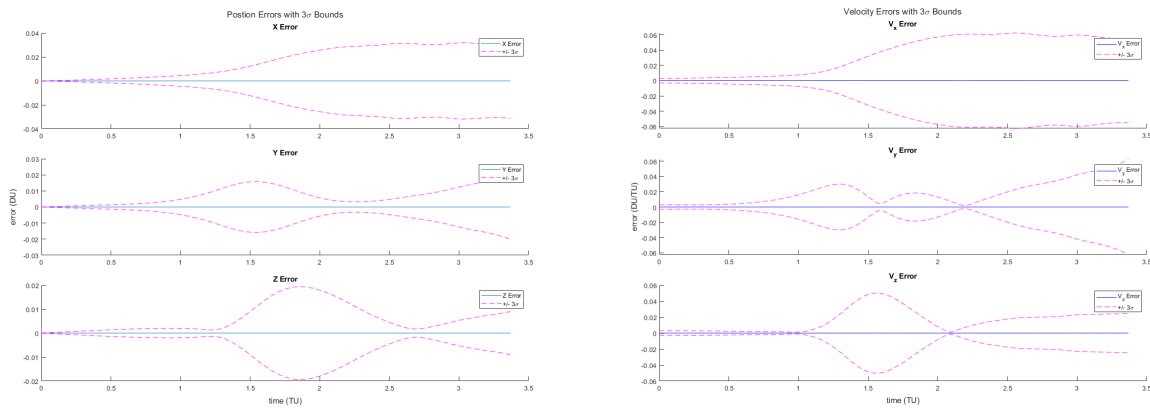


Fig. 12: Low Fidelity Error Orbit 1 - 12 Observers

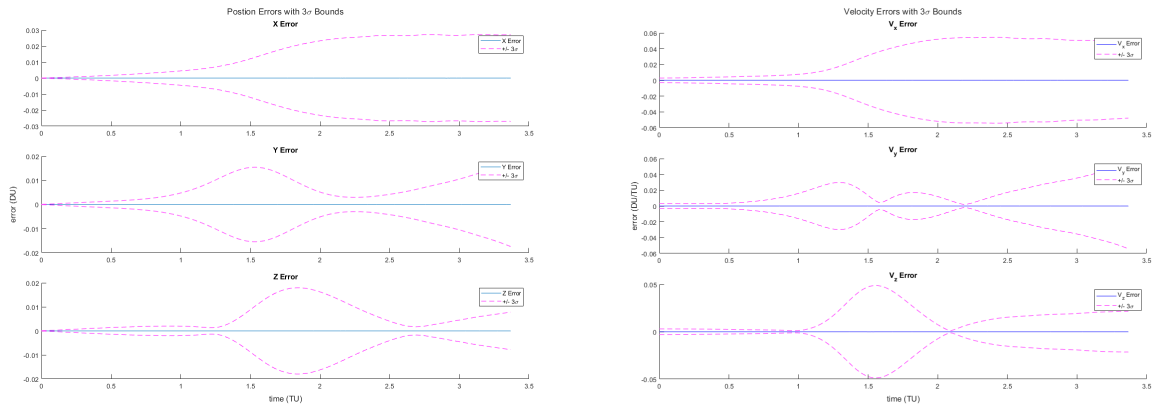


Fig. 13: Low Fidelity Error Orbit 1 - 16 Observers

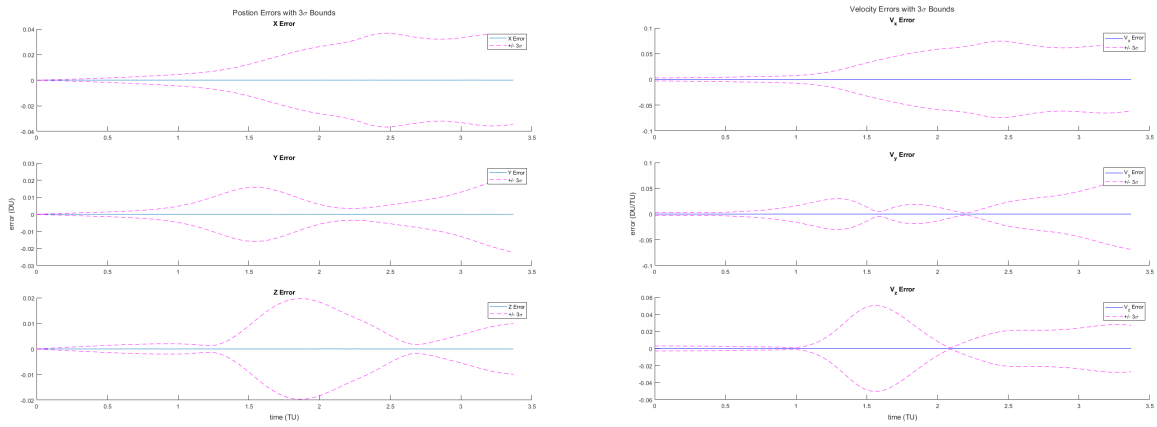


Fig. 14: Low Fidelity Error Orbit 2 - 8 Observers

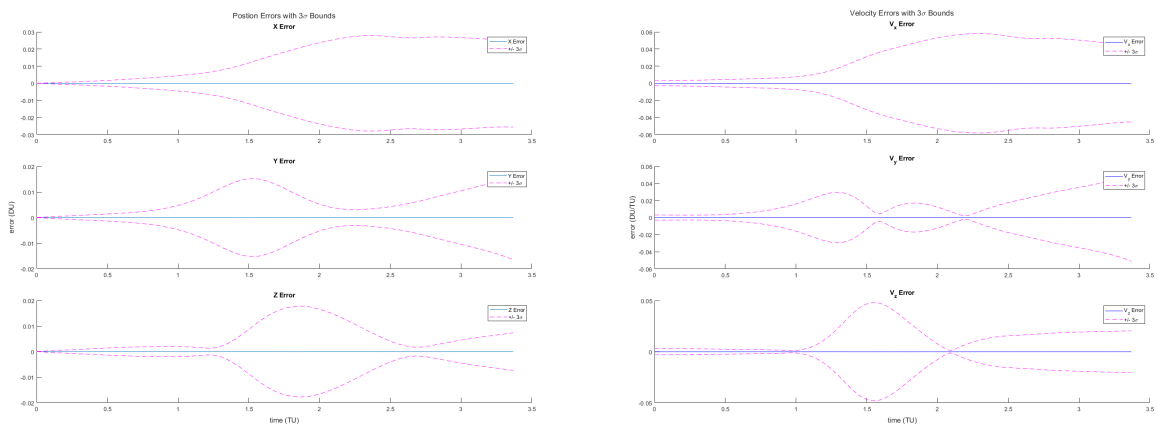


Fig. 15: Low Fidelity Error Orbit 2 - 12 Observers

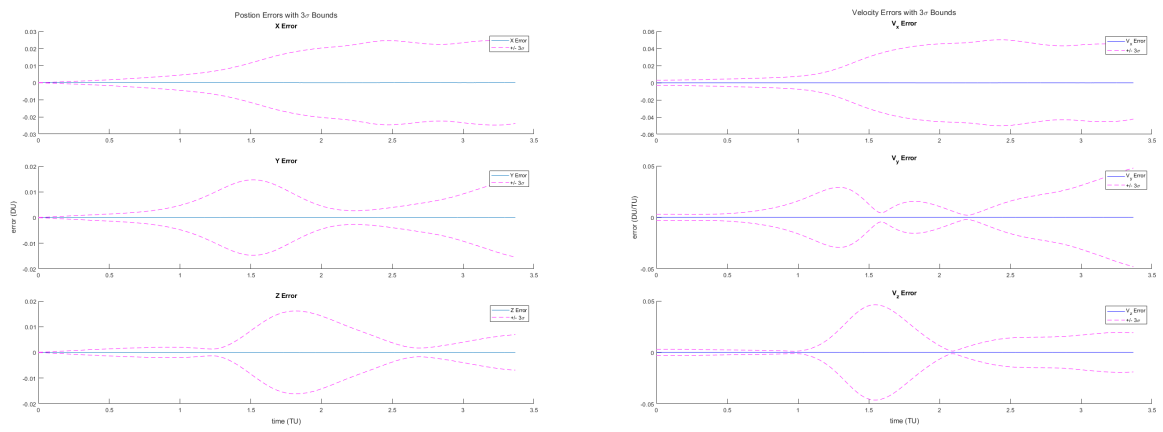


Fig. 16: Low Fidelity Error Orbit 2 - 16 Observers

The low fidelity cases also were able to generate a good estimate of the orbit state, although with slightly more uncertainty, 20-80 meters depending on case, than the high fidelity system. The RMSE values for the low fidelity test cases can be found in Table 7:

Table 7: Low Fidelity RMSE Values Non-Dimensionalized w/ Conversion

Case	Orbit 1		Orbit 2	
	$RMS_{pos}(km)$	$RMS_{vel}(km/s)$	$RMS_{pos}(km)$	$RMS_{vel}(km/s)$
8 Obs	5.1312e-07 (0.2006)	1.1027e-06 (1.1204e-06)	2.5264e-07 (0.0988)	6.2514e-07 (6.3516e-07)
12 Obs	1.5882e-07 (0.0621)	4.0263e-07 (4.0908e-07)	1.0489e-07 (0.0410)	1.5829e-07 (1.6083e-07)
16 Obs	1.8570e-07 (0.0726)	3.4927e-07 (3.5487e-07)	2.6453e-07 (0.1034)	5.2913e-07 (5.3761e-07)

3.3 Analysis

One interesting aspect of the values collected is how the RMSE values will occasionally increase between cases when observers are added. This is contrary to expectation, the RMSE value would presumably decrease when adding more measurements to the system. One reason why this is thought to occur is due to the noise being applied to the measurements and the general noise of the system. A preliminary analysis shows that the RMSE value varies according to random measurement noise seeding. This would seem to suggest that the variation in RMSE values between test cases is within the random noise of the method and does not represent a difference due to factor variation. More testing and stochastic analysis will be accomplished to investigate this further.

Figure 17 showcases the RMSE for both position and velocity in km and km/s respectively next to each other for each observer case.

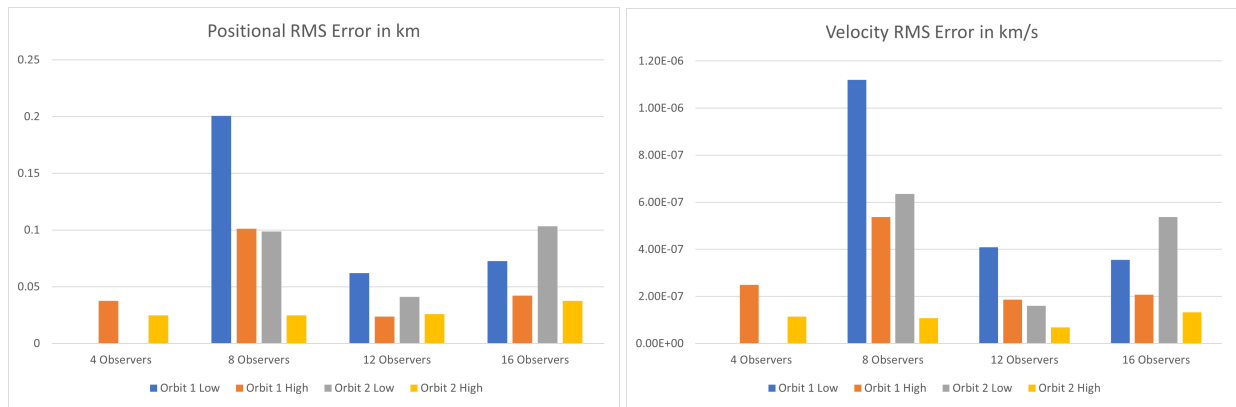


Fig. 17: RMSE Comparison for Position and Velocity

The best case for the low fidelity systems appears to be a constellation in Orbit 2 utilizing 12 observers. When compared with the high fidelity cases, it was able to match or exceed some of them by 61 meters in one case. Next to the best case of the high fidelity system, a constellation in Orbit 1 with 12 observers, there was only an RMSE difference of about 17 meters. These values seem to suggest that the use of a low fidelity system can in fact be used in lieu of a constellation of high fidelity systems. These RMSE values are also of a similar order of magnitude as those found in a recent study [10] using an EKF for orbit determination with Near Rectilinear Halo Orbits.

4. CONCLUSIONS AND FUTURE WORK

With the ever expanding focus on activities near the Moon and beyond, tracking objects within the cislunar domain is going to become as essential as modern applications of SDA and space traffic management are for near Earth operations today. The analysis done in this work helps to expand on previous research with the same periodic observation orbits. The application of an EKF shows the potential usefulness of both of the orbits used in this analysis in a SDA architecture. When looking at the implementation of different sensor packages for orbit prediction with this setup, the

low fidelity platforms, while not completely eclipsing the high fidelity platforms, showed they can perform the mission to a similar degree. This would allow for the use of a larger constellation of lower cost spacecraft when compared to high fidelity SDA systems. While further analysis is needed to quantitatively assess factor effects on RMSE, this study gives a good preliminary look into the performance of these type of SDA architectures.

Although some promising results are demonstrated, additional work should be done to further expand on this problem. While only two periodic orbits from the initial study [11] were investigated, it would be useful to look into testing with more of the periodic orbits, along with some different target orbits. In addition to adding additional observer and target orbits, combining multiple different observer orbits could also produce some interesting results. Another aspect of this work that could be further investigated is the constraints applied to the sensor for target detection. The constraints applied here were fairly simplistic and using a metric such as visual magnitude of the target when viewed from the observer would be useful in creating a more realistic measurement model. This is what was used in [11, 12]. Finally, the application of different kinds of filters to this problem would also help showcase their potential value for SDA. A batch filter would be particularly interesting to see how measurements collected from these orbits perform when doing initial orbit determination.

5. REFERENCES

- [1] R. F. Arenstorf. Existence of periodic solutions passing near both masses of the restricted three-body problem. *AIAA Journal*, 1:238–240, 1963.
- [2] R. F. Arenstorf. Periodic trajectories passing near both masses of the restricted three-body problem. In *Proceedings of the XIV International Astronautical Congress*, pages 85–97, 1963.
- [3] N. Bradley, Z. Olikara, S. Bhaskaran, and B. Young. Cislunar navigation accuracy using optical observations of natural and artificial targets. *Journal of Spacecraft and Rockets*, 57(4), July-August 2020.
- [4] Erin E Fowler, Stella B Hurtt, and Derek A Paley. Observability metrics for space-based cislunar domain awareness. In *AAS/AIAA Astrodynamics Specialist Conference*, 2020.
- [5] C. Frueh, K. Howell, K. J. DeMars, S. Bhadauria, and M. Gupta. Cislunar space traffic management: Surveillance through earth-moon resonance orbits. *8th European Conference on Space Debris*, 2021.
- [6] T. Gill. Nasa’s lunar orbital platform-gatwa unar orbital platform-gatway. In *The Space Congress® Proceedings*, 2018.
- [7] M. Gupta, K. C. Howell, and C. Frueh. Earth-moon multi-body orbits to facilitate cislunar surveillance activities. In *AIAA/AAS Astrodynamics Specialist Conference*, 2021.
- [8] C. Harris, D. Thomas, J. Kadan, K. Schroeder, and J. Black. Expanding the space surveillance network with space-based sensors using metaheuristic optimization techniques. In *The Advanced Maui Optical and Space Surveillance Technologies (AMOS) Conference*, Maui, HI, 2021.
- [9] M. Lo and S. Ross. The lunar 11 gateway: Portal to the stars and beyond. In *AIAA Space 2001 Conference and Exposition*, 2001.
- [10] Michael R Thompson, Anthony J Zara, Connor Ott, Matthew Bolliger, Ethan Kayser, and Diane C Davis. Comparisons of filtering algorithms for orbit determination in near rectilinear halo orbits. In *AAS/AIAA Astrodynamics Specialist Conference*, 2022.
- [11] A. Wilmer. Space domain awareness assessment of cislunar periodic orbits for lagrange point surveillance. Master’s thesis, Air Force Institute of Technology, 2021.
- [12] A. Wilmer, R. Bettinger, and B. Little. Preliminary viability assessment of cislunar periodic orbits for space domain awareness. In *The Advanced Maui Optical and Space Surveillance Technologies (AMOS) Conference*, Maui, HI, 2021.